Photon-assisted extrinsic Weyl orbits and three-dimensional quantum Hall effect in surface-doped topological Dirac semimetals

Zhi-Xian Kong, Zhang-Ze Xiong, Wei-Jing Wang ⓞ, Hou-Jian Duan,
Mou Yang ⓞ, Ming-Xun Deng ⓞ,*, and Rui-Qiang Wang†

Guangdong Basic Research Center of Excellence for Structure and Fundamental Interactions of Matter,
Guangdong Provincial Key Laboratory of Quantum Engineering and Quantum Materials, School of Physics,
South China Normal University, Guangzhou 510006, China
and Guangdong-Hong Kong Joint Laboratory of Quantum Matter, Frontier Research Institute for Physics,
South China Normal University, Guangzhou 510006, China

In this study, we investigate the manipulation of Weyl orbits in topological Dirac semimetals (DSMs) with surface doping using circularly polarized light (CPL). Our investigation reveals that surface impurities in topological DSMs can couple the Fermi arcs from different Weyl sectors, leading to the breakdown of intrinsic Weyl orbits. The application of CPL can effectively reduce the overlapping between the Fermi arcs, thereby restoring partial Fermi arcs of the topological DSMs. Subsequently, extrinsic Weyl orbits emerge between opposite Weyl sectors. These extrinsic Weyl orbits present an intriguing pathway to regulate the three-dimensional (3D) quantum Hall effect(QHE). The 3D QHE induced by the extrinsic Weyl orbits can be modulated through surface magnetic perturbations and light irradiation, resulting in observable quantized Hall plateaus in the parameter space of CPL. Our findings propose a promising approach for stabilizing Weyl orbits and manipulating the 3D QHE in topological semimetals.

I. INTRODUCTION

Weyl semimetals (WSMs) belong to the family of topological semimetals, renowned for hosting low-energy Weyl fermion excitations characterized by well-defined chirality near the Weyl nodes [1–9] . The Weyl nodes exist in pairs of opposite chiralities [10,11], serving as sources and sinks of the Berry curvature, and are connected by nonclosed Fermi arcs in momentum space. Recently, a three-dimensional (3D) quantum Hall effect (QHE) because of Fermi arcs was proposed in WSMs [12], which has sparked significant theoretical [13–26] and experimental [27–31] activities in condensed matter physics.

The QHE, traditionally observed in 2D systems like the 2D electron gas [32,33], faces challenges in 3D due to the extra dimension along the magnetic field direction, hindering the quantization of Hall conductivity. However, several inherent properties enable a 3D WSM to support the QHE. First, the Weyl orbits, comprising Fermi arcs from opposite surfaces, can form cyclotron orbits crucial for the QHE. This arrangement facilitates Weyl fermion tunneling between Fermi arcs at opposing surfaces via the Weyl nodes. Second, a notable depletion of bulk carriers occurs as the Fermi energy approaches the Weyl nodes, where the bulk density of states reduces significantly for the unique electronic structure of WSMs. Finally, the bending of the surface energy contour can lead to the formation of a 2D electron gas by the Fermi arcs. Due to

a peculiar absence of conventional bulk-boundary correspondence, WSM Hall bars can exhibit an unconventional fully 3D anisotropy in the QHE [24]. Interestingly, the cyclotron orbits in WSMs can take nontrivial knotting structures such as a trefoil knot, which offers an arena of the nontrivial knot theory in three spatial dimensions and its subsequent physical consequences [34].

The 3D QHE via the Weyl-orbit mechanism has been experimentally observed in topological Dirac semimetals (DSMs) [27–31], where the quantized Hall conductivity exhibits sensitivity to sample thickness [29]. A topological DSM hosts paired gap-closing points known as Dirac points, stabilized by time-reversal, spatial-inversion, and crystalline symmetries. If the time-reversal or spatial-inversion symmetry is broken, a single Dirac point can be split into a pair of Weyl nodes with opposite chiralities, causing a topological transition from a Dirac to a Weyl semimetal [35–40]. Topological DSMs, such as Cd_3As_2 [41] and A_3Bi ($A = $ Na, K, Rb) [42], can be viewed as two overlapping copies of a WSM, which possess two sets of surface Fermi arcs in the surface Brillouin zone. Consequently, for a topological DSM slab, a single surface possesses two Fermi arcs, forming a closed Weyl loop.

In topological DSMs, the presence of Fermi loops on the same surface can lead to the deformation of Weyl orbits by perturbations, rendering them unstable [43–45]. For instance, the inclusion of a bulk higher-order momentum term can induce Lifshitz transitions in the Fermi arc surface states, potentially disrupting the Weyl orbits without breaking the system's symmetry [45]. Moreover, the overlap of Fermi arcs from distinct Weyl sectors on the same surface exacerbates

the susceptibility of Weyl orbits to surface perturbations, amplifying their inherent instability. However, the Weyl nodes, serving as endpoints of the Fermi arcs, are expected to remain immune to surface perturbations due to their protection by bulk topology. Given that the Fermi arcs and bulk Weyl nodes collaboratively contribute to the construction of Weyl orbits, both bulk and surface perturbations can influence the Weyl-orbit-induced 3D QHE. Notably, surface perturbations are more accessible to manipulation in experiments compared to bulk perturbations. Given these considerations, it is natural to inquire whether stable Weyl orbits and 3D QHE can persist in the presence of surface perturbations. If not, urgent additional investigation is needed to develop strategies for stabilizing these phenomena within topological DSMs.

In this work, we apply a beam of circularly polarized light (CPL), a widely adopted technique for inducing topological phase transitions in materials [46–53], to manipulate Weyl orbits in surface-doped topological DSMs. We find that the Fermi arcs can be coupled by surface perturbations, which breaks down the intrinsic Weyl orbits. The application of CPL enables the restoration of partial Fermi arcs by significantly reducing the overlapping region within the surface spectrum. While the intrinsic Weyl orbits are broken by surface magnetic impurities, extrinsic Weyl orbits can be established between the opposite Weyl sectors, which suggests an interesting routine to realize and modulate the 3D QHE. The 3D QHE arising from the extrinsic Weyl orbits can manifest in variation of the quantized Hall conductivity with the CPL's parameters. The rest of this paper is organized as follows. In Sec. II, we derive the effective Hamiltonian from the Floquet theory, and discuss the off-resonant-light-dressed bulk spectrum. In Sec. III, we numerically investigate the phonon-modulated Fermi arc surface states by mapping the effective Hamiltonian into a tight-binding form. The phonon-assisted extrinsic Weyl orbits, and the 3D QHE induced by extrinsic Weyl orbits are discussed respectively in Sec. IV and Sec. V. The last section contains a concise summary.

II. EFFECTIVE HAMILTONIAN AND BULK SPECTRUM

We consider a 3D topological DSM subjected to both light and magnetic fields, as sketched by Fig. 1(a), which can be described by the effective Hamiltonian (see Appendix A):

$$
\begin{aligned}
\mathcal{H}_{\text{eff}}(\boldsymbol{k}) = &(\hbar \upsilon_{\text{F}} + \lambda_2 \sigma_z)(k_x \sigma_z \tau_x - k_y \tau_y) \\
&- \lambda_1 k_z (\cos \phi \tau_x - \sin \phi \sigma_z \tau_y) \\
&+ (m_{\boldsymbol{k}} - m_A + \lambda_F \sigma_z) \tau_z.
\end{aligned} \tag{1}
$$

Specifically, $m_A = [(1 + \varsigma^2)m_2 + (m_1 - m_2)\sin^2 \theta] k_A^2 / 2$, $\lambda_F = \varsigma \hbar \upsilon_{\text{F}}^2 k_A^2 \cos \theta / \omega$, $\lambda_1 = 2\varsigma m_1 \upsilon_{\text{F}} k_A^2 \sin \theta / \omega$, $\lambda_2 = 2\varsigma m_2 \upsilon_{\text{F}} k_A^2 \cos \theta / \omega$, and $k_A = e\mathcal{A}/\hbar$ characterizes the irradiation intensity. The symbols ω, $\mathcal{A}$, and ς (= 0, ±1) are employed to represent the frequency, amplitude and (linear, right/left circular) polarization of the light, respectively. Since $[\sigma_z, \mathcal{H}_{\text{eff}}(\boldsymbol{k})] = 0$, the effective Hamiltonian can be written in the block-diagonalized form as $\mathcal{H}_{\text{eff}}(\boldsymbol{k}) = \text{diag}[\mathcal{H}_{\text{eff}}^+(\boldsymbol{k}), \mathcal{H}_{\text{eff}}^-(\boldsymbol{k})]$, where

$$
\mathcal{H}_{\text{eff}}^s(\boldsymbol{k}) = \lambda_s (s k_{x,s} \tau_x - k_{y,s} \tau_y) + m_{\boldsymbol{k},s} \tau_z, \tag{2}
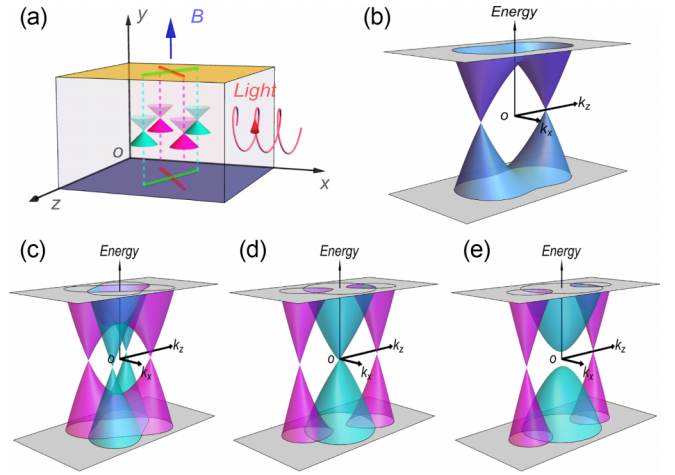$$

FIG. 1. (a) Schematic for a topological DSM subjected to both light and magnetic fields, where the color-filled cones represent the bulk dispersion, with wine red (sky blue) for the spin up (down) sector, and the lines on the surfaces that connect the projection of the bulk Weyl nodes denote the Fermi arcs. The blue arrow accounts for the applied magnetic field. (b) Static spectrum of the topological DSM and (c)–(e) photon-modulated spectrum for $k_y = 0$, $\hbar \omega = 2$, $k_A = 1$, $\phi = 0$, and (c) $\theta = \pi/2$, (d) $\theta = \pi/5$, and (e) $\theta = 0$. The parameters of the topological DSM are set as $m_0 = 1$, $m_1 = 0.6$, $m_2 = 0.5$, and $\hbar \upsilon_{\text{F}} = 1$.

and $s = \pm 1$ is the eigenvalue of σ_z. Here, $\lambda_s = \hbar \upsilon_{\text{F}} + s\lambda_2$, $k_{x,s} = k_x - s\frac{\lambda_1}{\lambda_s} k_z \cos \phi$, $k_{y,s} = k_y - s\frac{\lambda_1}{\lambda_s} k_z \sin \phi$, and $m_{\boldsymbol{k},s} = m_s - m_1 k_z^2 - m_2 (k_x^2 + k_y^2)$ with $m_s = m_0 - m_A + s\lambda_F$.

In the absence of the magnetic field, $\boldsymbol{k}$ is a good quntum number, such that we can diagonalize Eq. (2) in the plane-wave basis and obtain the bulk dispersion

$$
\varepsilon_{\boldsymbol{k},\eta}^s = \eta \sqrt{\lambda_s^2 (k_{x,s}^2 + k_{y,s}^2) + m_{\boldsymbol{k},s}^2}, \tag{3}
$$

where $\eta = \pm$ corresponds to the conduction/valence band. Without the light, the bulk spectrum is spin degenerate, as shown by Fig. 1(b). The evolution of the bulk spectrum with the light's propagation direction is depicted in Figs. 1(c)–1(e). For $m_s > 0$, the bulk dispersion will form a Weyl cone around the Weyl node

$$
\boldsymbol{K}_\chi^s = \chi k_w^s \left(s\frac{\lambda_1}{\lambda_s} \cos \phi, s\frac{\lambda_1}{\lambda_s} \sin \phi, 1 \right), \tag{4}
$$

where $\chi = \pm 1$ and $k_w^s = \sqrt{m_s / (m_1 + m_2 \lambda_1^2 / \lambda_s^2)}$. Since the parameters $\lambda_F, \lambda_{1,2} \propto \varsigma k_A^2 / \omega$ are coupled with the spin, the degeneracy of the bulk Weyl nodes can be eliminated by CPL, but can not by linearly polarized light. If $|\lambda_F| < m_A$, namely,

$$
\frac{m_1 - m_2}{2} \cos^2 \theta + \frac{\hbar \upsilon_{\text{F}}^2}{\omega} \cos \theta < \frac{m_1 + \varsigma^2 m_2}{2}, \tag{5}
$$

m_s decreases with increasing the irradiation intensity, such that a pair of Weyl nodes can merge at $\boldsymbol{k} = 0$ when $m_s = 0$, and be gapped out when $m_s < 0$. In the opposite regime where $|\lambda_F| > m_A$, m_s can decrease for one spin sector and increase for the other as the irradiation intensity changes, and as a result, the Weyl nodes for the two spin sectors will be shifted by the CPL to opposite directions. The relative magnitudes

of $|\lambda_F|$ and m_A are controllable by adjusting the frequency or/and incident direction of the light, demonstrated by Eq. (5), making the bulk spectrum tunable by the direction of the light, as observed in Figs. 1(c)–1(e). Because the projection of the bulk Weyl nodes on the surfaces are connected by Fermi arcs, the Fermi arcs can be modulated by the light. Notably, when the CPL is incident away from the direction of z, the bulk Weyl nodes are not aligned on the same line, as depicted in Fig. 1(c), which can prevent the overlap of Fermi arcs. Hence, it is expected that Weyl orbits will exhibit sensitivity to the CPL, thereby enabling the tunability of the 3D QHE through irradiation.

III. PHOTON-MODULATED FERMI ARC SURFACE STATES

When the sample is confined between $y = \pm L_y/2$, we can analytically derive the low-energy surface spectrum in the x-z plane [45]

$$\mathcal{H}_{\text{surf}}^{s\beta}(k_x, k_z) = -s\beta\lambda_s k_x - \beta\lambda_1 k_z \cos\phi, \qquad (6)$$

where $k_z \in [-k_w^s, k_w^s]$ and $\beta = \pm$ corresponds to the top/bottom surface. Accordingly, at the Fermi level $E_F = 0$, we can determine the Fermi arcs $k_x = -s\lambda_1 k_z \cos\phi/\lambda_s$. Without the light, the Fermi arcs from different spin sectors overlap at $k_x = 0$ and $k_z \in [-k_w^s, k_w^s]$. Due to the overlapping, the Fermi arcs can be easily coupled by surface magnetic perturbations. The overlapping region can be reduced when the CPL is applied. For example, as the CPL is incident away from the y-z plane, i.e., $\theta \neq 0$ and $\phi \neq \pi/2$, the Fermi arcs, instead of overlapping, will intersect only at $k_x = k_z = 0$. In this sense, the CPL can be utilized to stabilize and engineer the Fermi arcs of topological DSMs.

To further demonstrate how the Fermi arc surface states are modified by the off-resonant light and surface perturbations, we perform numerical calculations by mapping Eq. (1) to a 1D lattice Hamiltonian (see Appendix B)

$$H_0 = \sum_m c_m^\dagger (h_0 c_m + h_y c_{m+1} + h_y^\dagger c_{m-1}), \qquad (7)$$

in which $h_0 = f_0 + f_1 \cos k_z - f_z \sin k_z + f_2 \cos k_x + f_x \sin k_x$, and $h_y = (f_2 + if_y)/2$. Here, we noted $f_0 = (m_0 - m_A + \lambda_F \sigma_z)\tau_z - f_1 - 2f_2$, $f_{1(2)} = 2m_{1(2)}\tau_z$, $f_{x(y)} = (\hbar \upsilon_F \sigma_z + \lambda_2)\sigma_{0(z)}\tau_{x(y)}$, and $f_z = \lambda_1(\tau_x \cos\phi - \sigma_z \tau_y \sin\phi)$. The disordered effect can be modeled by a set of randomly distributed impurity potentials, namely, $\mathcal{V}_{kk'} = \sum_m V_m e^{-i(k-k')\cdot R_m}$ with $V_m = V_0\sigma_0 + V_M s_m \cdot \sigma$ and s_m as the direction vector of the impurity's local magnetic moment. For diluted doping, the disordered effect can be dealt with using the T-matrix approach, where the impurity potentials are incorporated into the self-energy

$$\Sigma_k(\epsilon) = \left[\mathbf{1} - \bar{\mathcal{V}}_k \frac{1}{N} \sum_q g_q(\epsilon)\right]^{-1} \bar{\mathcal{V}}_k, \qquad (8)$$

and subsequently enter the retarded Green's function

$$\mathcal{G}_k^r(\epsilon) = [1 - g_k(\epsilon)\Sigma_k(\epsilon)]^{-1} g_k(\epsilon). \qquad (9)$$

Here, $\bar{\mathcal{V}}_k = \frac{1}{N}\sum_{k'}\langle \mathcal{V}_{kk'}\rangle_{\text{dis}}$ means disordered average of the impurity potentials and $g_k(\epsilon) = (\epsilon + i0^+ - H_0)^{-1}$ represents the impurity-free retarded Green's function.

From the retarded Green's function, we can determine the k-resolved density of states (DOSs),

$$\rho(\epsilon, k_x, k_z) = -\frac{1}{\pi}\text{Tr}\{\text{Im}[\mathcal{G}_k^r(\epsilon)]\}, \qquad (10)$$

which allows us to show the impurity-perturbed bulk states and surface Fermi arcs, simultaneously. In Fig. 2, we display the k-resolved DOSs, where asymmetric surface magnetic perturbation $V_m = V_M \sigma_x(\delta_{m,1} + \delta_{m,N_y}/2)$ is adopted to eliminate the degeneracy of the spectra, completely. From Figs. 2(a) and 2(e), we observe that in the absence of light and magnetic perturbation, the Fermi arcs at $E_F = 0$ overlap at $k_x = 0$ and $k_z \in [-k_w^s, k_w^s]$. The overlapping Fermi lines are quite sensitive to surface magnetic impurities, as shown by Fig. 2(b), where the surface spectrum repel each other and open a gap for finite V_M. As a result, the Fermi arcs reduce to two Fermi points at $E_F = 0$, as demonstrated by Fig. 2(f). When the CPL is applied in direction z, the overlapping region between the Fermi arcs of different spin sectors decreases, leading to the restoration of partial Fermi arcs, as depicted in Figs. 2(c) and 2(g). If the CPL is incident in the x direction, the surface spectra become k_z dependent and coupled by the surface magnetic doping, see Fig. 2(d). Consequently, two surface Fermi pockets emerge around the Fermi surface, causing the Fermi arcs of different spin sectors to form a closed Fermi loop, as observed in Fig. 2(h). The behaviors of the Fermi arcs are consistent with the analytical results.

IV. PHOTON-ASSISTED EXTRINSIC WEYL ORBITS

As discussed above, the Fermi arcs in topological DSMs can be destroyed by surface magnetic doping, rendering their Weyl orbits unstable. Conversely, the Fermi arcs are adjustable through CPL, providing a viable means to manipulate and stabilize the Weyl orbits. To demonstrate this point, we establish the Weyl orbits by applying a magnetic field along the y direction, denoted by $A(r) = -Bx\hat{e}_z$. After the Peierls substitution $k_z \to k_z - \frac{eB}{\hbar}x$, the Hamiltonian becomes x dependent, so that we need to further discretize Eq. (7) using the Fourier transform $c_m = \sum_n e^{-ik_x x_n} c_{m,n}$. Subsequently, we can arrive at the square lattice model

$$H_0 = \sum_{mn} c_{m,n}^\dagger (h_n c_{m,n} + h_x c_{m,n+1} + h_y c_{m+1,n}) + \text{H.c.} \qquad (11)$$

with $h_n = (f_0 + f_1 \cos\xi_n + f_z \sin\xi_n)/2$ and $h_x = (f_2 - if_x)/2$. Here, we noted $\xi_n = (x_n - \ell_B^2 k_z)/\ell_B^2$ and $\ell_B = \sqrt{\hbar/|eB|}$ is the magnetic length.

By diagonalizing Eq. (11), we can obtain the Landau levels (LLs) and wavefunctions, referred to as ε_{j,k_z} and $\psi_{j,k_z}(x, y)$, respectively. Accordingly, we can define the local electron probability density $P_j(x, y, k_z) = |\psi_{j,k_z}(x, y)|^2$. The LLs and spatial distribution of the electron probability density are presented in Fig. 3. In the Weyl-orbit mechanism, the surface fermions driven by the magnetic field will move along the Fermi arcs from one Weyl valley to the other and tunnel to opposite surfaces at the Weyl nodes via bulk states. Therefore, the Weyl orbits manifest in the probability density as a bright
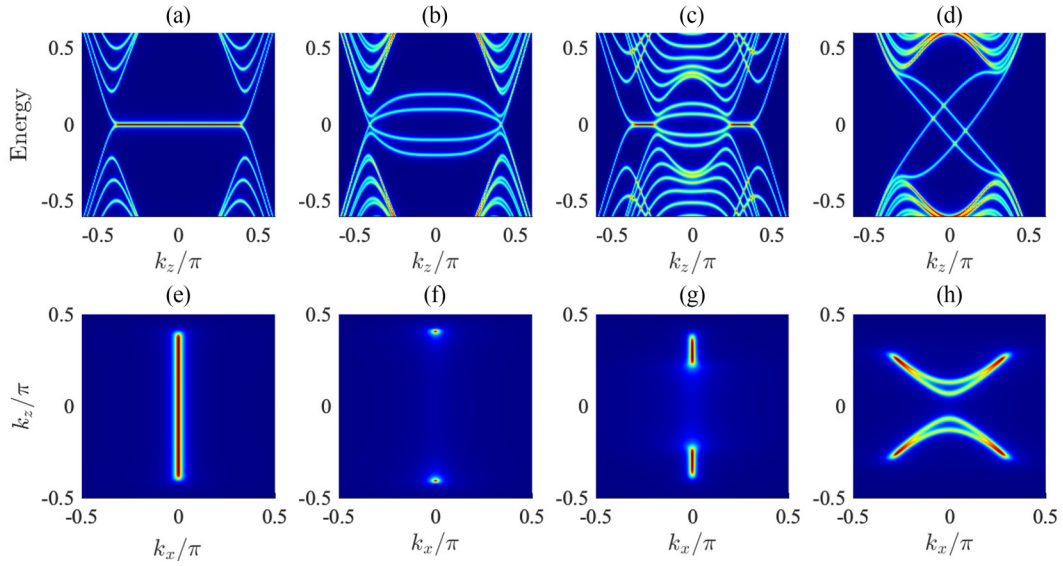
FIG. 2. Evolution of the **k**-resolved DOSs (a)–(d) $\rho(\epsilon, k_x = 0, k_z)$ and (e)–(h) $\rho(\epsilon = 0, k_x, k_z)$, denoted by the filled colors, for $(V_M, k_A, \theta) = (0, 0, 0)$, $(0.2, 0, 0)$, $(0.2, 0.8, 0)$, and $(0.2, 0.8, \pi/2)$. Here, $\varsigma = 1$, $\phi = 0$, $N_y = 20$, and other parameters are the same as Fig. 1.

closed loop, as seen from Fig. 3(e), where two bright stripes cross the bulk and connect the surface states at opposite surfaces. The width of the stripes $\sim 2\ell_B$ relates to the cyclotron radius of the bulk Weyl fermions, and the distance between the stripes encodes the momentum distance between the two Weyl nodes. When the Weyl fermions travel along the Fermi arcs from one Weyl node to the other, their cyclotron center

will change by $\Delta x_c = 2\ell_B^2 k_w^s$, which is exactly the distance between the two bright stripes.

From Figs. 3(a) and 3(e), it can be observed that the LLs resulting from the Weyl-orbit mechanism are uniformly spaced. When the Fermi arcs are impeded by surface impurities, the intrinsic Weyl orbits will break down, as evidenced in Fig. 3(f), where the electron probability density is
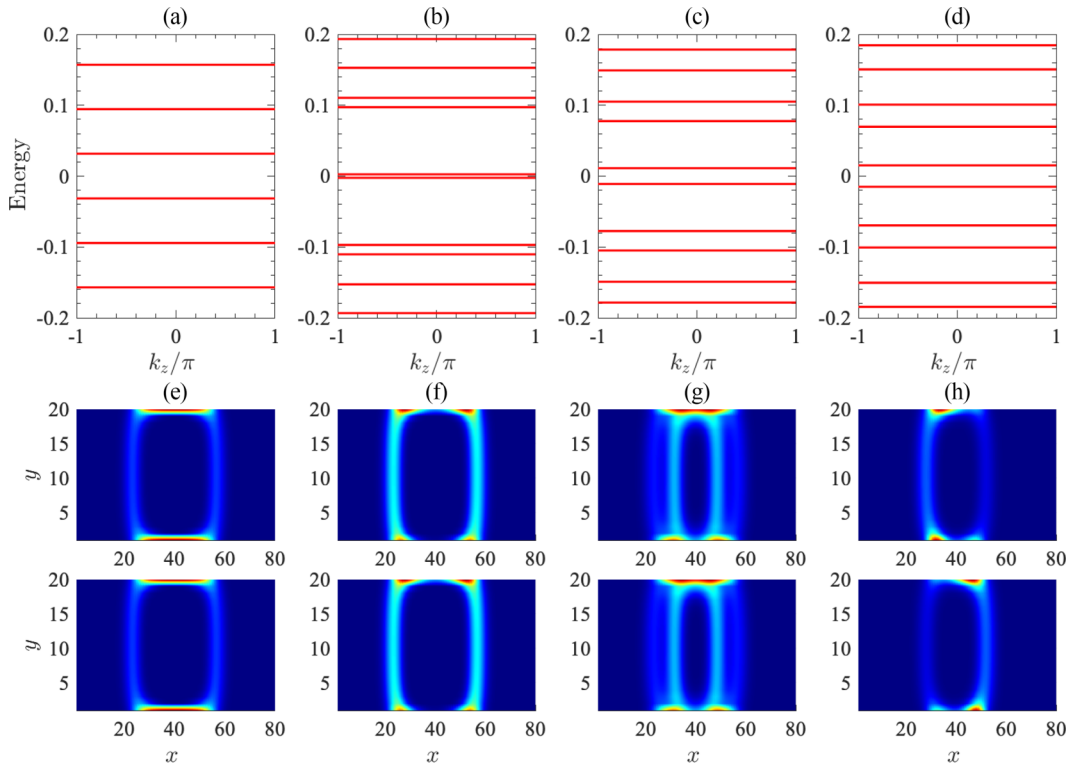

FIG. 3. (a)–(d) The LLs and (e)–(h) spatial distribution of the electron probability density $P_j(x, y, \pi)$ for $j = 2N_xN_y + 1$ and $j = 2N_xN_y$, respectively, in the upper and lower panels, with $(V_M, k_A, \theta) = (0, 0, 0)$, $(0.2, 0, 0)$, $(0.2, 0.8, 0)$, and $(0.2, 0.8, \pi/2)$. Here, we set $N_x = 80$, $\ell_B = \sqrt{N_x/2\pi}$, and other parameters the same as Fig. 2.
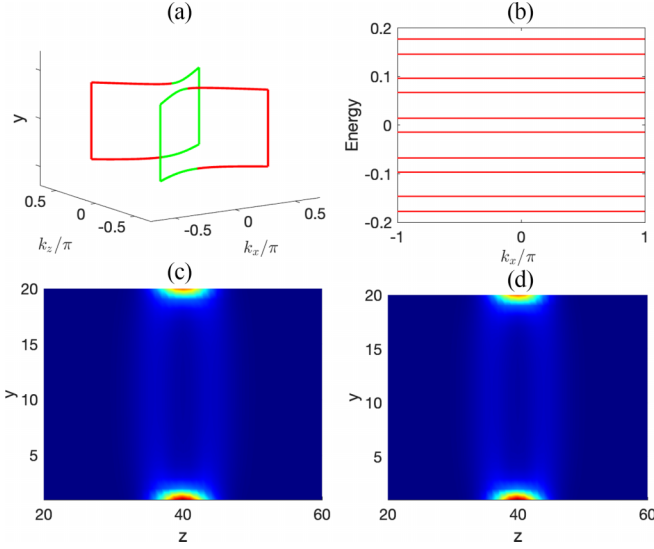
FIG. 4. (a) Schematic of the extrinsic Weyl orbits. (b) LLs calculated with the vector potential $A(r) = Bz\hat{e}_x$. (c), (d) Spatial distribution of the electron probability density $P_j(y, z, \pi)$ for $j = 2N_y N_z$ and $j = 2N_y N_z + 1$, respectively. The parameters are the same as Fig. 3.

discontinuous in the surface and enhanced in the bulk. As a consequence, the LLs undergo significant alterations, making them irregularly spaced, as depicted in Fig. 3(b). Interestingly, while the intrinsic Weyl orbits are broken, extrinsic Weyl orbits can form between different spin sectors when the Fermi arcs are partially reinstated by CPL, as indicated by the two lateral bright loops in Fig. 3(g). The extrinsic Weyl orbits can be observed more clearly when the CPL is incident in direction x, in which case the Fermi arcs from different spin sectors form a closed Fermi loop, as exemplified in Fig. 2(h). Therefore, the LLs regain regular spacing, but the probability density distribution is notably different from those of the intrinsic Weyl orbits, as shown by Fig. 3(h). The extrinsic Weyl orbits can be observed in the y-z plane, when the magnetic field is gauged by the vector potential $A(r) = Bz\hat{e}_x$, as shown by Fig. 4. The splitting of the LLs in Figs. 2(b)–2(d) is attributed to the asymmetric surface magnetic doping. For symmetric surface magnetic doping, e.g., $V_m = V_M \sigma_x(\delta_{m,1} - \delta_{m,N_y})$, the spectrum of the upper and lower surfaces are identical, and the LLs will return to be doublet degenerate.

V. 3D QHE INDUCED BY THE EXTRINSIC WEYL ORBITS

To better understand the 3D QHE related to the Weyl orbits, we derive the Hall conductivity analytically before conducting numerical calculations. For simplicity, it is assumed that the light is incident in direction z, such that the light-introduced parameters can be reduced as $\lambda_1 = 0$, $\lambda_2 = 2\varsigma m_2 \upsilon_F k_A^2/\omega$, $\lambda_F = \varsigma \hbar \upsilon_F^2 k_A^2/\omega$, and $m_A = (1 + \varsigma^2)m_2 k_A^2/2$. Upon application of the magnetic field, we can expand Eq. (2) around $\mathbf{K}_\chi^s$ as

$$\mathcal{H}_{\text{eff}}^{s\chi}(\mathbf{k}) = \hbar\omega_s(\chi\xi\tau_z - is\partial_\xi\tau_x) - \lambda_s k_y \tau_y, \quad (12)$$

where $\xi = \sqrt{\lambda_z \lambda_s^{-1}}(x - \ell_B^2 k_z)/\ell_B$ is a dimensionless quantity with $\lambda_z = 2m_1 k_w^s$, and $\omega_s = \sqrt{\lambda_z \lambda_s}/(\hbar\ell_B)$ represents the cyclotron frequency. Subsequently, we can determine the eigenvalues

$$\varepsilon_{n,k_y}^{s\chi} = \begin{cases} -s\chi\lambda_s k_y & n = 0 \\ s_n\sqrt{2n(\hbar\omega_s)^2 + \lambda_s^2 k_y^2} & n \neq 0 \end{cases}, \quad (13)$$

and the wavefunctions in the τ_y representation read

$$\Psi_{0,k_y}^{s\chi} = (1 + s\chi, 1 - s\chi)^T/2, \quad (14)$$

$$\Psi_{n\neq0,k_y}^{s\chi} = \frac{1}{\sqrt{2}}\begin{pmatrix} \chi\sqrt{1 - \frac{\lambda_s k_y}{\varepsilon_{k_y,n}^{s\chi}}}\phi_{|n|-\frac{1-s\chi}{2}} \\ s_n\sqrt{1 + \frac{\lambda_s k_y}{\varepsilon_{k_y,n}^{s\chi}}}\phi_{|n|-\frac{1+s\chi}{2}} \end{pmatrix}, \quad (15)$$

where $s_n = \text{sgn}(n)$ and $\phi_{|n|}$ is the harmonic oscillator wavefunction.

For the low-energy continuum Hamiltonian (12), k_y remains a good quantum number and we can calculate the k_y-resolved Hall conductivity via the Kubo formula [12–16]

$$\sigma_{xz}^{s\chi}(k_y) = \frac{ie^2\hbar}{2\pi\ell_B^2}\sum_{mn}\frac{(f_n^{s\chi} - f_m^{s\chi})\hat{v}_{x,mn}^{s\chi}\hat{v}_{z,nm}^{s\chi}}{(\varepsilon_{m,k_y}^{s\chi} - \varepsilon_{n,k_y}^{s\chi})^2}, \quad (16)$$

where $\hat{v}_{\alpha,mn}^{s\chi} = \langle\Psi_{m,k_y}^{s\chi}|\hbar^{-1}\partial_{k_\alpha}\mathcal{H}_{\text{eff}}^{s\chi}(\mathbf{k})|\Psi_{n,k_y}^{s\chi}\rangle$ denotes the velocity matrix element and $f_n^{s\chi} = f(\varepsilon_{n,k_y}^{s\chi})$ with $f(\epsilon) = 1/[1 + \exp(\frac{\epsilon-E_F}{k_B T})]$ being the Fermi-Dirac distribution function. By substituting Eqs. (13)–(15) into Eq. (16), and after some tedious algebra, we can arrive at

$$\sigma_{xz}^{s\chi}(k_y) = \frac{e^2}{h}\sum_{n=0}^{\infty}\left(n + \frac{1}{2}\right)(f_n^{s\chi} - f_{n+1}^{s\chi} + f_{-n}^{s\chi} - f_{-n-1}^{s\chi}). \quad (17)$$

As evident from Eq. (17), $\sigma_{xz}^{s\chi}(k_y)$ is quantized for a given $k_y = k_0$. However, the dispersion with continuous k_y would prevent the quantization of the total Hall conductivity $\sigma_{xz}^s = \sum_{\chi,k_y}\sigma_{xz}^{s\chi}(k_y)$.

In the following, we take $s = 1$ for the purpose of illustration. The LLs and $\sigma_{xz}^{s\chi}(k_0)$ are depicted in Figs. 5(a) and 5(b), where the chirality of the Weyl fermions is encoded in the $n = 0$ LLs. As observed, $\sigma_{xz}^{s\chi}(k_0) = (n + \frac{1}{2})e^2/h$ displays a series of plateaus and jumps by one unit of e^2/h whenever the Fermi level crosses the intersection points between the LLs and $k_y = k_0$. If $n = 0$ ($|n| \geq 1$), the solutions to $\varepsilon_{n,k_y}^{s\chi} = E_F$ are different (identical) for the two Weyl valleys, making $\sigma_{xz}^{s+}(k_0)$ equal (unequal) to $\sigma_{xz}^{s-}(k_0)$ when $|E_F|$ is greater (smaller) than $\sqrt{2}\hbar\omega_s$, as observed in Figs. 5(a) and 5(b). For $|E_F| < \sqrt{2}\hbar\omega_s$, after performing the summation in Eq. (17), the total Hall conductivity can be reduced to

$$\sigma_{xz}^s = \frac{e^2}{h}\sum_{k_y}[f(s\lambda_s k_y) + f(-s\lambda_s k_y) - 1]. \quad (18)$$

If k_y is consecutive, we can replace the summation with an integral $\sum_{k_y} \rightarrow \frac{L_y}{2\pi}\int dk_y$. Together with the approximation $f(\epsilon) \simeq \Theta(E_F - \epsilon)$ at low temperatures, where $\Theta(x)$ is the
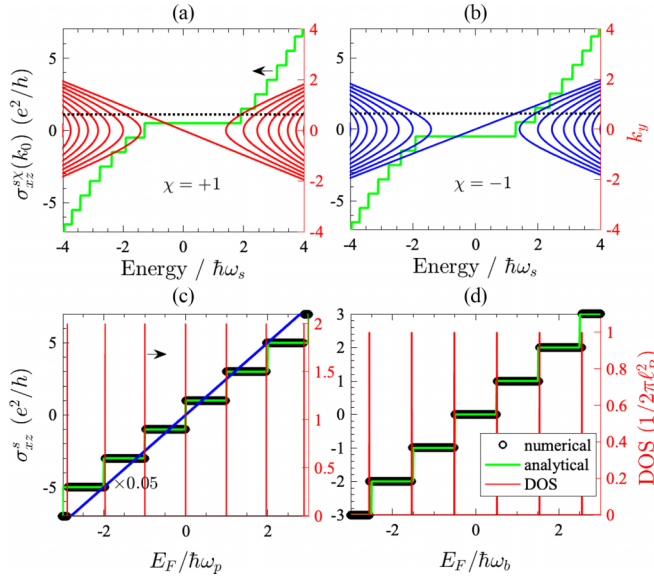
FIG. 5. (a), (b) Analytical results for the LLs (right axis) and the k_y-resolved Hall conductivity $\sigma_{xz}^{s\chi}(k_0)$ (left axis) with $k_0 = 0.2$ (dotted lines), and (a) $\chi = +1$ and (b) $\chi = -1$, and the Hall conductivity σ_{xz}^s arises from the (c) periodic boundary condition and (d) Weyl-orbit mechanism. The blue line in (c) indicates the value of σ_{xz}^s for continuous k_y. Here, we set $s = 1$, $N_x = 40$, $N_y = 40$, and other parameters the same as Fig. 3.

unit step function, we can further derive Eq. (18) as $\sigma_{xz}^s = \frac{e^2}{h} \frac{E_F L_y}{\pi \lambda_s}$. Consequently, σ_{xz}^s changes continuously and is linearly scaled with E_F, as indicated by the blue line in Fig. 5(c). This insight suggests that if k_y is discretized, quantized Hall conductivity would become observable.

Theoretically, the simplest way to discretize k_y is to suppose the periodic boundary condition in direction y, i.e., $k_y L_y = 2n_y\pi$ with $n_y \in \mathbb{Z}$. After that, the LLs in Eq. (13) become $\varepsilon_{n,n_y}^{s\chi} = \varepsilon_{n,k_y \to 2n_y\pi/L_y}^{s\chi}$, and the Hall conductivity will exhibit a plateau when the Fermi level is within the gap between $\varepsilon_{n,n_y}^{s\chi}$ and $\varepsilon_{n,n_y+1}^{s\chi}$. As a result, when $\hbar\omega_p = 2\pi\lambda_s/L_y \ll \hbar\omega_s$ and $|E_F| < \sqrt{2}\hbar\omega_s$, the Hall conductivity will be quantized as

$$\sigma_{xz}^s = \text{sign}(E_F)(2\mathcal{N}_p + 1)\frac{e^2}{h} \tag{19}$$

with $\mathcal{N}_p = \lfloor\frac{|E_F|}{\hbar\omega_p}\rfloor$, where $\lfloor x \rfloor$ means x rounded downwards to the nearest integer, shown by the green curve in Fig. 5(c). For the mechanism of periodic boundary conditions, there is always a LL at $E_F = 0$, which corresponds to $n_y = 0$, leading to a jump in the Hall conductivity, as illustrated in Fig. 5(c). Additionally, the LLs exhibit doublet degeneracy because the two Weyl valleys are quantized independently. Since $\hbar\omega_p$ is magnetic independent, the Hall conductivity in Fig. 5(c) does not rely on the magnetic field.

The Weyl orbits provide another interesting mechanism for the quantization. As mentioned above, in the Weyl-orbit mechanism, the surface fermions, driven by the magnetic field, will move along the Fermi arcs unidirectionally from one Weyl valley to the other, and then tunnel to the opposite surface at the Weyl nodes via the bulk states, and finally

return to its initial position. The dynamic phase for such a Weyl orbit can be derived as $\Delta\varphi_s = \sum_{\chi\beta}(\chi k_y L_y + \beta k_x \Delta x_c)$. Analogous to the periodic boundary condition, the dynamic phase satisfies the quantization condition $\Delta\varphi = (2n+1)\pi$, where the additional π phase arises from the noncommutation between k_x and $k_z - x/\ell_B^2$. This is known as the Sommerfeld quantization condition in quantum mechanics. For a given energy $|E| < \sqrt{2}\hbar\omega_s$, we can determine $k_x = -s\beta E/\lambda_s$ and $k_y = -s\chi E/\lambda_s$, respectively, from the surface spectrum in Eq. (6) and the $n = 0$ bulk LLs in Eq. (13). Then, by substituting the expressions of k_x and k_y into the quantization condition, we can immediately obtain the discrete spectrum $E_n^s = s(n + \frac{1}{2})\hbar\omega_b$ with

$$\hbar\omega_b = \frac{\pi\lambda_s}{L_y + 2\ell_B^2 k_w^s}. \tag{20}$$

Distinct from the mechanism of periodic boundary conditions, the spectrum quantization here is jointly realized by the two Weyl valleys, so that the LLs in Fig. 5(d) are singlet degenerate. As a result, the Hall conductivity takes on a distinct form

$$\sigma_{xz}^s = \text{sgn}(E_F)\mathcal{N}_b\frac{e^2}{h} \tag{21}$$

with $\mathcal{N}_b = \lfloor\frac{|E_F|}{\hbar\omega_b} + \frac{1}{2}\rfloor$. Besides, as a result of the additional π phase, $\mathcal{N}_b$ can not reach zero, and there is no LL at $E_F = 0$.

To proceed, we conduct numerical calculations directly from the lattice Hamiltonian (11) to corroborate the described physical picture. In terms of the LLs ε_{j,k_z} and wavefunctions ψ_{j,k_z} mentioned below Eq. (11), the Kubo formula can be reexpressed as [45]

$$\sigma_{xz} = \frac{2e^2\hbar}{L_x L_z} \sum_{k_z, i \neq j} \frac{\text{Im}(\hat{v}_{x,ij}\hat{v}_{z,ji})}{(\varepsilon_{j,k_z} - \varepsilon_{i,k_z})^2} f(\varepsilon_{i,k_z}) \tag{22}$$

with $\hat{v}_{\alpha,ij} = \langle\psi_{i,k_z}|\hat{v}_\alpha|\psi_{j,k_z}\rangle$, where the velocity operators are defined by $\hat{v}_x = i\hbar^{-1}\sum_{mn}[H, x_m c_{m,n}^\dagger c_{m,n}]$ and $\hat{v}_z = \partial H/(\hbar\partial k_z)$. Without magnetic perturbations, the spin sectors are decoupled and the Hall conductivity can be calculated separately for $s = \pm 1$. To compare with analytical results, we present numerical results for the spin-resolved Hall conductivity in Figs. 5(c) and 5(d), as marked by the dark circles. Observationally, the results obtained from the analytical and numerical approaches exhibit significant agreement, which confirms the proposed physical picture regarding the LLs and 3D QHE.

In Fig. 6, we present the Hall conductivity corresponding to the LLs in Fig. 3. According to the physical picture above, we can easily understand the behaviors of the LLs and the resulting Hall conductivity. As depicted in Fig. 3(a), in the absence of surface magnetic perturbation, the LLs remain degenerate for the two spin species. Consequently, the Hall conductivity exhibits a steplike behavior, increasing by two units of e^2/h whenever the Fermi level traverses the LLs. When the intrinsic Weyl orbits are disrupted by surface magnetic doping, LLs can develop around zero energy, in analogy to the situation with periodic boundaries. Therefore, the Hall conductivity can display odd plateaus, as observed in Fig. 3(b), where
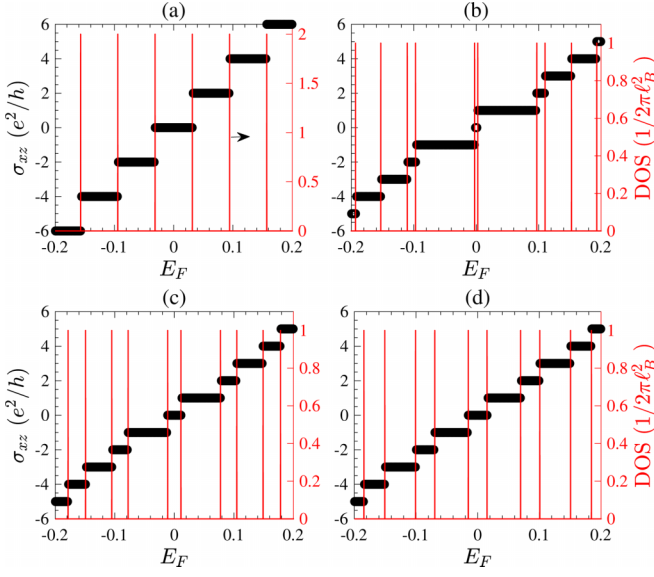
FIG. 6. The Hall conductivity σ_{xz} (left axis) and DOS (right axis) for the LLs in Figs. 3(a)–3(d).

FIG. 7. Evolution of the Hall conductivity σ_{xz} with the parameters of the CPL, for (a) $\theta = 0$, $V_M = 0$, (b) $k_A = 0.5$, $V_M = 0$, (c) $\theta = 0$, $V_M = 0.2$, and (d) $k_A = 0.5$, $V_M = 0.2$. The rest of the parameters are set the same as Fig. 6.

the height of the Hall conductivity steps reduces to one unit of e^2/h, for the degeneracy of the LLs is eliminated by the surface magnetic impurities. As the CPL is activated, extrinsic Weyl orbits would be established between the two spin sectors, leading to the restoration of regular Hall plateaus, illustrated by Figs. 3(c) and 3(d). However, the decreasing dynamic phase from the Fermi arcs will result in an increase in $\hbar\omega_b$, and thus in the width of the Hall plateaus, in comparison to Fig. 3(a). Interestingly, since the extrinsic Weyl orbits are sensitive to the light irradiation, the 3D QHE can be observable by varying the parameters of CPL, as demonstrated by Fig. 7.

In practice, Dirac and Weyl semimetals exhibit opacity due to the skin effect in conductors, and the penetration depth of light is a critical factor to consider. Experimental data shows that the penetration depth of light in WSMs can extend to hundreds of nanometers, as demonstrated in Ref. [54], where a depth of 750 nm was reported. This value significantly exceeds the typical sample thickness (approximately 100 nm) used to observe the 3D quantum Hall effect, as noted in Ref. [29]. Therefore, the penetration depth of light can adequately cover the length scale relevant to Weyl orbits. On the other hand, boundary effects in the x or z directions may influence the penetration depth of light, involving phenomena such as reflection, refraction, absorption, scattering, surface plasmons, etc. How their effects influence the photon-induced external Weyl orbits needs further exploration.

VI. SUMMARY

We studied the Weyl-orbit-induced 3D QHE in surface-doped topological DSMs. It is found that the intrinsic Weyl orbits in topological DSMs can be destroyed by surface magnetic doping, and the related 3D QHE will break down. Upon application of CPL, extrinsic Weyl orbits can be established, which is constructed by the Fermi arcs from opposite Weyl sectors, due to t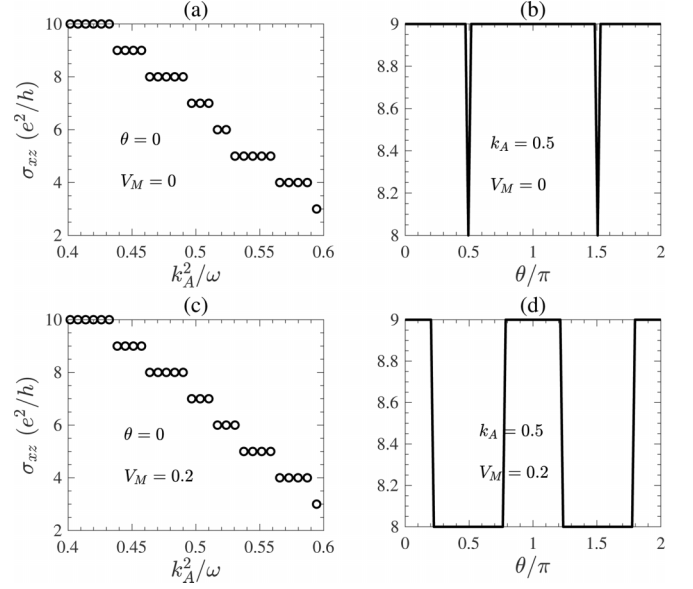he coupling of the Fermi arcs by surface impurities. The extrinsic Weyl orbits can not only be modulated by the irradiation intensity, but also by the irradiation direction of the light, making the 3D QHE observable by varying the parameters of the CPL. Our findings provide a perspective for stabilizing Weyl orbits and exploring the 3D QHE in topological semimetals.

APPENDIX A: DERIVATION FOR THE EFFECTIVE HAMILTONIAN

The static topological DSM accommodates two copies of WSMs with opposite spin polarizations, which can be described by the widely adopted Hamiltonian

$$\mathcal{H}(\boldsymbol{k}) = \hbar \upsilon_{\mathrm{F}}(k_x \sigma_z \tau_x - k_y \tau_y) + m_{\boldsymbol{k}} \tau_z. \tag{A1}$$

Here, $\tau_{\alpha=x,y,z}$ (σ_α) represents the Pauli matrix acting on the orbital (spin) subspace, υ_{F} denotes the Fermi velocity, and $m_{\boldsymbol{k}} = m_0 - m_1 k_z^2 - m_2(k_x^2 + k_y^2)$ with $m_{0,1,2} > 0$ as the model parameter. The light and magnetic fields can be included by a vector potential, i.e., $\boldsymbol{E}(t) = -\partial_t \boldsymbol{A}$ and $\boldsymbol{B} = \nabla \times \boldsymbol{A}$, which enters the Hamiltonian via the Peierls substitution $\boldsymbol{k} \to \boldsymbol{k} + e\boldsymbol{A}/\hbar$. For the combined light and magnetic fields, the vector potential can take the form $\boldsymbol{A} = \boldsymbol{A}(\boldsymbol{r}) + \boldsymbol{A}(t)$, where

$A(r)$ captures the magnetic field, and $A(t) = \mathcal{A}[\cos(\omega t)\hat{e}_x + \varsigma\sin(\omega t)\hat{e}_y]\hat{\mathcal{R}}(\theta,\phi)$ accounts for a light beam incident in the direction of $\boldsymbol{n} = \hat{e}_z\hat{\mathcal{R}}(\theta,\phi) = (\sin\theta\cos\phi, \sin\theta\sin\phi, \cos\theta)$. The symbols ω, $\mathcal{A}$, and $\varsigma\,(=0,\pm1)$ are employed to represent the frequency, amplitude, and (linear, right/left circular) polarization of the light, respectively. Here, the rotation operator $\hat{\mathcal{R}}(\theta,\phi)$ can be represented by a matrix

$$\hat{\mathcal{R}}(\theta,\phi) = \begin{pmatrix} \cos\theta\cos\phi & \cos\theta\sin\phi & -\sin\theta \\ -\sin\phi & \cos\phi & 0 \\ \sin\theta\cos\phi & \sin\theta\sin\phi & \cos\theta \end{pmatrix}, \quad \text{(A2)}$$

which aligns the x (z) axis of the coordinate system with the light's initial polarization (propagation) direction.

We would focus on the off-resonant regime where $\hbar\omega$ is much greater than the width of the static energy band. In this situation, the absorption and emission of real photons are suppressed. However, the energy band can still be modified through virtual photon absorption and emission processes. The off-resonant-light-dressed Hamiltonian can be determined by the Floquet theorem [46–53]

$$\mathcal{H}_{\text{eff}}(\boldsymbol{k}) = \mathcal{H}(\boldsymbol{k}) + \sum_{n>0}\frac{1}{n\hbar\omega}[\mathcal{H}_n, \mathcal{H}_{-n}], \quad \text{(A3)}$$

where $\boldsymbol{k} = -i\boldsymbol{\nabla} + eA(\boldsymbol{r})/\hbar$ and $\mathcal{H}_n = \frac{\omega}{2\pi}\int_0^{2\pi/\omega}\mathcal{H}(\boldsymbol{k} + eA/\hbar)e^{-in\omega t}dt$. Accordingly, we can obtain the effective Hamiltonian presented in Eq. (1) of the main text.

APPENDIX B: DERIVATION FOR THE TIGHT-BINDING HAMILTONIAN

In the language of second quantization, the total Hamiltonian can be written as

$$H = \sum_{\boldsymbol{k}} c_{\boldsymbol{k}}^\dagger h(\boldsymbol{k})c_{\boldsymbol{k}} + \sum_{\boldsymbol{k}\boldsymbol{k}'} c_{\boldsymbol{k}}^\dagger \mathcal{V}_{\boldsymbol{k}\boldsymbol{k}'}c_{\boldsymbol{k}'}, \quad \text{(B1)}$$

where $c_{\boldsymbol{k}}^\dagger$ $(c_{\boldsymbol{k}})$ represents the electron creation (annihilation) operator, and the last term describes the disordered effect arising from impurity scattering. Concretely, The single-particle Hamiltonian $h(\boldsymbol{k})$ can be obtained from Eq. (1) directly by the transforms $k_\alpha \to \sin k_\alpha$ and $k_\alpha^2 \to 2 - 2\cos k_\alpha$, yielding

$$h(\boldsymbol{k}) = f_0 + f_1\cos k_z - f_z\sin k_z + f_2\cos k_x$$
$$+ f_x\sin k_x + f_2\cos k_y - f_y\sin k_y. \quad \text{(B2)}$$

Here, $f_0 = (m_0 - m_A + \lambda_F\sigma_z)\tau_z - f_1 - 2f_2$, $f_{1(2)} = 2m_{1(2)}\tau_z$, $f_{x(y)} = (\hbar v_F\sigma_z + \lambda_2)\sigma_{0(z)}\tau_{x(y)}$, and $f_z = \lambda_1(\tau_x\cos\phi - \sigma_z\tau_y\sin\phi)$. For the sample with finite size in the y direction, we can discretize the Hamiltonian by the Fourier transform $c_{\boldsymbol{k}} = \sum_m e^{-ik_y y_m}c_m$, and obtain the impurity-free 1D lattice Hamiltonian, as presented in Eq. (7) of the main texts.

[1] X. Wan, A. M. Turner, A. Vishwanath, and S. Y. Savrasov, Topological semimetal and fermi-arc surface states in the electronic structure of pyrochlore iridates, Phys. Rev. B **83**, 205101 (2011).

[2] A. A. Burkov and L. Balents, Weyl semimetal in a topological insulator multilayer, Phys. Rev. Lett. **107**, 127205 (2011).

[3] H. Weng, C. Fang, Z. Fang, B. A. Bernevig, and X. Dai, Weyl semimetal phase in noncentrosymmetric transition-metal monophosphides, Phys. Rev. X **5**, 011029 (2015).

[4] D. Pesin and A. H. MacDonald, Spintronics and pseudospintronics in graphene and topological insulators, Nat. Mater. **11**, 409 (2012).

[5] M. I. Katsnelson, K. S. Novoselov, and A. K. Geim, Chiral tunnelling and the Klein paradox in graphene, Nat. Phys. **2**, 620 (2006).

[6] B. Yan and C. Felser, Topological materials: Weyl semimetals, Annu. Rev. Condens. Matter Phys. **8**, 337 (2017).

[7] N. P. Armitage, E. J. Mele, and A. Vishwanath, Weyl and Dirac semimetals in three-dimensional solids, Rev. Mod. Phys. **90**, 015001 (2018).

[8] C.-K. Chiu, J. C. Y. Teo, A. P. Schnyder, and S. Ryu, Classification of topological quantum matter with symmetries, Rev. Mod. Phys. **88**, 035005 (2016).

[9] B. Q. Lv, T. Qian, and H. Ding, Experimental perspective on three-dimensional topological semimetals, Rev. Mod. Phys. **93**, 025002 (2021).

[10] H. Nielsen and M. Ninomiya, The Adler-Bell-Jackiw anomaly and Weyl fermions in a crystal, Phys. Lett. B **130**, 389 (1983).

[11] G. E. Volovik, *The Universe in a Helium Droplet* (Oxford University Press on Demand, Oxford, UK, 2003), Vol. 117.

[12] C. M. Wang, H.-P. Sun, H.-Z. Lu, and X. C. Xie, 3d quantum Hall effect of fermi arcs in topological semimetals, Phys. Rev. Lett. **119**, 136806 (2017).

[13] H. Li, H. Liu, H. Jiang, and X. C. Xie, 3d quantum Hall effect and a global picture of edge states in Weyl semimetals, Phys. Rev. Lett. **125**, 036602 (2020).

[14] R. Ma, D. N. Sheng, and L. Sheng, Three-dimensional quantum Hall effect and magnetothermoelectric properties in Weyl semimetals, Phys. Rev. B **104**, 075425 (2021).

[15] H. Geng, G. Y. Qi, L. Sheng, W. Chen, and D. Y. Xing, Theoretical study of the three-dimensional quantum Hall effect in a periodic electron system, Phys. Rev. B **104**, 205305 (2021).

[16] M. Chang, H. Geng, L. Sheng, and D. Y. Xing, Three-dimensional quantum Hall effect in Weyl semimetals, Phys. Rev. B **103**, 245434 (2021).

[17] M. Chang and L. Sheng, Three-dimensional quantum Hall effect in the excitonic phase of a Weyl semimetal, Phys. Rev. B **103**, 245409 (2021).

[18] H.-Z. Lu, 3d quantum Hall effect, Natl. Sci. Rev. **6**, 208 (2019).

[19] S. Li, C. Wang, Z. Du, F. Qin, H.-Z. Lu, and X. Xie, 3d quantum Hall effects and nonlinear Hall effect, npj Quantum Mater. **6**, 96 (2021).

[20] F. Qin, S. Li, Z. Z. Du, C. M. Wang, W. Zhang, D. Yu, H.-Z. Lu, and X. C. Xie, Theory for the charge-density-wave mechanism of 3d quantum Hall effect, Phys. Rev. Lett. **125**, 206601 (2020).

[21] J. Gooth, S. Galeski, and T. Meng, Quantum-hall physics and three dimensions, Rep. Prog. Phys. **86**, 044501 (2023).

[22] Y.-X. Wang and Z. Cai, Quantum oscillations and three-dimensional quantum Hall effect in ZrTe$_5$, Phys. Rev. B **107**, 125203 (2023).

[23] Z. Du, C. Wang, H.-P. Sun, H.-Z. Lu, and X. Xie, Quantum theory of the nonlinear Hall effect, Nat. Commun. **12**, 5038 (2021).

[24] X.-X. Zhang and N. Nagaosa, Anisotropic three-dimensional quantum Hall effect and magnetotransport in mesoscopic Weyl semimetals, Nano Lett. **22**, 3033 (2022).

[25] R. Chen, T. Liu, C. M. Wang, H.-Z. Lu, and X. C. Xie, Field-tunable one-sided higher-order topological hinge states in Dirac semimetals, Phys. Rev. Lett. **127**, 066801 (2021).

[26] R. Chen, C. M. Wang, T. Liu, H.-Z. Lu, and X. C. Xie, Quantum Hall effect originated from helical edge states in Cd$_3$As$_2$, Phys. Rev. Res. **3**, 033227 (2021).

[27] M. Uchida, Y. Nakazawa, S. Nishihaya, K. Akiba, M. Kriener, Y. Kozuka, A. Miyake, Y. Taguchi, M. Tokunaga, N. Nagaosa *et al.*, Quantum Hall states observed in thin films of Dirac semimetal Cd$_3$As$_2$, Nat. Commun. **8**, 2274 (2017).

[28] T. Schumann, L. Galletti, D. A. Kealhofer, H. Kim, M. Goyal, and S. Stemmer, Observation of the quantum Hall effect in confined films of the three-dimensional Dirac semimetal Cd$_3$As$_2$, Phys. Rev. Lett. **120**, 016801 (2018).

[29] C. Zhang, Y. Zhang, X. Yuan, S. Lu, J. Zhang, A. Narayan, Y. Liu, H. Zhang, Z. Ni, R. Liu *et al.*, Quantum Hall effect based on Weyl orbits in Cd$_3$As$_2$, Nature (London) **565**, 331 (2019).

[30] F. Tang, Y. Ren, P. Wang, R. Zhong, J. Schneeloch, S. A. Yang, K. Yang, P. A. Lee, G. Gu, Z. Qiao *et al.*, Three-dimensional quantum Hall effect and metal–insulator transition in ZrTe$_5$, Nature (London) **569**, 537 (2019).

[31] B.-C. Lin, S. Wang, S. Wiedmann, J.-M. Lu, W.-Z. Zheng, D. Yu, and Z.-M. Liao, Observation of an odd-integer quantum Hall effect from topological surface states in Cd$_3$As$_2$, Phys. Rev. Lett. **122**, 036602 (2019).

[32] K. V. Klitzing, G. Dorda, and M. Pepper, New method for high-accuracy determination of the fine-structure constant based on quantized Hall resistance, Phys. Rev. Lett. **45**, 494 (1980).

[33] D. J. Thouless, M. Kohmoto, M. P. Nightingale, and M. den Nijs, Quantized Hall conductance in a two-dimensional periodic potential, Phys. Rev. Lett. **49**, 405 (1982).

[34] Y. Zhang, Cyclotron orbit knot and tunable-field quantum Hall effect, Phys. Rev. Res. **1**, 022005(R) (2019).

[35] S. Raza, A. Sirota, and J. C. Y. Teo, From Dirac semimetals to topological phases in three dimensions: A coupled-wire construction, Phys. Rev. X **9**, 011039 (2019).

[36] A. A. Zyuzin, S. Wu, and A. A. Burkov, Weyl semimetal with broken time reversal and inversion symmetries, Phys. Rev. B **85**, 165110 (2012).

[37] P. Goswami and S. Tewari, Axionic field theory of $(3 + 1)$-dimensional Weyl semimetals, Phys. Rev. B **88**, 245107 (2013).

[38] S. E. Han, G. Y. Cho, and E.-G. Moon, Quantum criticality with infinite anisotropy in topological phase transitions between Dirac and Weyl semimetals, Phys. Rev. B **98**, 085149 (2018).

[39] M.-X. Deng, W. Luo, R.-Q. Wang, L. Sheng, and D. Y. Xing, Weyl semimetal induced from a Dirac semimetal by magnetic doping, Phys. Rev. B **96**, 155141 (2017).

[40] C. Chen, Z.-M. Yu, S. Li, Z. Chen, X.-L. Sheng, and S. A. Yang, Weyl-loop half-metal in li$_3$(FeO$_3$)$_2$, Phys. Rev. B **99**, 075131 (2019).

[41] Z. Wang, H. Weng, Q. Wu, X. Dai, and Z. Fang, Three-dimensional Dirac semimetal and quantum transport in Cd$_3$As$_2$, Phys. Rev. B **88**, 125427 (2013).

[42] Z. Wang, Y. Sun, X.-Q. Chen, C. Franchini, G. Xu, H. Weng, X. Dai, and Z. Fang, Dirac semimetal and topological phase transitions in A_3bi ($a =$ Na, k, rb), Phys. Rev. B **85**, 195320 (2012).

[43] M. Kargarian, M. Randeria, and Y.-M. Lu, Are the surface fermi arcs in Dirac semimetals topologically protected? Proc. Natl. Acad. Sci. USA **113**, 8648 (2016).

[44] Z. Yan, Z. Wu, and W. Huang, Vortex end majorana zero modes in superconducting Dirac and Weyl semimetals, Phys. Rev. Lett. **124**, 257001 (2020).

[45] T.-R. Qin, Z.-H. Chen, T.-X. Liu, F.-Y. Chen, H.-J. Duan, M.-X. Deng, and R.-Q. Wang, Quantum Hall effect in topological Dirac semimetals modulated by the lifshitz transition of the fermi arc surface states, Phys. Rev. B **109**, 125111 (2024).

[46] M. S. Rudner, N. H. Lindner, E. Berg, and M. Levin, Anomalous edge states and the bulk-edge correspondence for periodically driven two-dimensional systems, Phys. Rev. X **3**, 031005 (2013).

[47] P. Titum, N. H. Lindner, M. C. Rechtsman, and G. Refael, Disorder-induced Floquet topological insulators, Phys. Rev. Lett. **114**, 056801 (2015).

[48] A. Farrell and T. Pereg-Barnea, Photon-inhibited topological transport in quantum well heterostructures, Phys. Rev. Lett. **115**, 106403 (2015).

[49] C.-K. Chan, P. A. Lee, K. S. Burch, J. H. Han, and Y. Ran, When chiral photons meet chiral fermions: Photoinduced anomalous Hall effects in Weyl semimetals, Phys. Rev. Lett. **116**, 026805 (2016).

[50] Z. Yan and Z. Wang, Tunable Weyl points in periodically driven nodal line semimetals, Phys. Rev. Lett. **117**, 087402 (2016).

[51] M.-X. Deng, W. Y. Deng, D. X. Shao, R.-Q. Wang, R. Shen, L. Sheng, and D. Y. Xing, Photon-modulated impurity scattering on a topological insulator surface, Phys. Rev. B **95**, 115102 (2017).

[52] P.-H. Fu, H.-J. Duan, R.-Q. Wang, and H. Chen, Phase transitions in three-dimensional Dirac semimetal induced by off-resonant circularly polarized light, Phys. Lett. A **381**, 3499 (2017).

[53] X.-S. Li, C. Wang, M.-X. Deng, H.-J. Duan, P.-H. Fu, R.-Q. Wang, L. Sheng, and D. Y. Xing, Photon-induced Weyl half-metal phase and spin filter effect from topological Dirac semimetals, Phys. Rev. Lett. **123**, 206601 (2019).

[54] G. B. Osterhoudt, L. K. Diebel, M. J. Gray, X. Yang, J. Stanco, X. Huang, B. Shen, N. Ni, P. J. W. Moll, Y. Ran, and K. S. Burch, Colossal mid-infrared bulk photovoltaic effect in a type-I Weyl semimetal, Nat. Mater. **18**, 471 (2019).